Single shot generation of high-aspect-ratio nano-rods from sapphire by ultrafast first order Bessel beam

Valeria Viviana Belloni [1] (*), Mostafa Hassan [1], Luca Furfaro [1], Remo Giust [1], Anne-Magali Seydoux-Guillaume [2], Sergio Sao-Joao [3], and Francois Courvoisier [1](*)
[1] FEMTO-ST institute, Univ. Franche-Comté and CNRS, 15B avenue des Montboucons, 25030 Besançon, France.
[2] UJM, CNRS, LGL-TPE, F-42023, Saint Etienne, France
[3] Mines Saint-Etienne, Univ. Lyon, CNRS, UMR 5307 LGF, Centre SMS, F-42023 Saint-Etienne, France

This article has been published in open access in *Laser & Photonics Reviews*.
Its full reference is:
”Single Shot Generation of High-Aspect-Ratio Nano-Rods from Sapphire by Ultrafast First Order Bessel Beam,” V. V. Belloni, M. Hassan, L. Furfaro, R. Giust, A.-M. Seydoux-Guillaume, S. Sao-Joao, F. Courvoisier, *Laser & Photonics Reviews*, 2300687 (2023). `https://doi.org/10.1002/lpor.202300687`

Engineering the polarization and spatial phase of ultrafast laser pulses represents a compelling strategy for enhancing control over laser-matter interaction and enabling rapid and innovative nano-fabrication processes. Here, we report the single-shot, ultrafast laser fabrication of high-aspect-ratio, vertically standing nano-pillars with a diameter of approximately 800 nm and height up to 15 μm on the surface of sapphire. To achieve this, we harnessed the distinctive properties of diffraction-free, first-order Bessel beams endowed with either radial or azimuthal polarization distributions, under tight focusing conditions. The highly intense laser-matter interaction in this configuration generates a tubular-shaped, high-pressure field beneath the material surface, leading to the rapid expulsion of material across the surface. We identified three distinct regimes and a mechanism, based on the Rayleigh-Plateau theory, that explains the distinct morphological regimes observed. Our findings not only shed light on the underlying physical mechanisms of intense excitation of transparent dielectrics but also offer exciting prospects for the rapid fabrication of positive nano-structures and material compression across various fields of application.

1 Introduction

Integration of innovative beam, polarization and temporal shaping has yielded remarkable progress in the field of material processing, enabling precise manipulation of matter [1–5]. Specifically, radial polarization has emerged as a particularly appealing approach for laser drilling since it favors the phenomenon of resonance absorption, which enhances the efficient transfer of energy from the laser to the material surface [6,7]. The ability to control polarization patterns across the beam empowers a wide variety of sophisticated textures both on the surface and within the bulk of materials [8,9]. For instance, by exerting control over the local polarization orientation, complex orientation patterns of laser-induced periodic surface structures can be precisely tailored, while the plasmonic field enhancement induced by polarization plays a significant role in determining the depth of these structures [10,11]. Additionally, beams featuring polarization states that evolve during propagation have enabled the fabrication of chiral structures within the bulk of fused silica [12].

Optical vortices have also emerged as effective tools for manipulating laser-matter interaction. In Gaussian laser beams, the phase singularity is responsible for doughnut-shaped cross-sections. Interestingly, the vortex carried by the optical pulse can be transferred to the material, resulting in the generation of nano-needles with helical surface sub-structures on tantalum [13,14], silicon [15], silver [16], and aluminum [17] through single-shot ablation. Vortex beams have also been employed to create other intricate structures such as nano-domes [18], three-dimensional chiral structures [19], and spiraling fibers [20].

Bessel beams offer a fascinating class of solutions to the Helmholtz equation due to their inherent propagation invariance [21,22]. Unlike Gaussian beams, Bessel beams exhibit an extended focal region that surpasses the equivalent Rayleigh range by several orders of magnitude. A zeroth-order Bessel beam is a cylindrically-symmetric interference field that can be produced using an axicon [23] or a spatial light modulator [24]. For sufficiently high focusing angles, the nonlinear propagation of ultrashort pulses inside transparent dielectrics is highly stable with negligible influence from the nonlinear Kerr effect [25]. This regime allows for energy deposition of a single ultrashort pulse along a high-aspect ratio nano-plasma, which evolves within tens of microseconds [26], into a high-aspect ratio nano-void inside glasses or sapphire, with important applications for high-speed cutting ($\sim$ 1 m/s) or for the nano-fabrication of sensors [27–33].

Importantly, higher-order Bessel beams, which carry a vortex charge, possess a focal region in the shape of a high-aspect-ratio hollow cylinder. Their stability in the nonlinear, ultrashort pulse regime has been demonstrated [34]. The violent material phase change produced in the wake of the single shot laser illumination inside transparent dielectrics [35], emitting shockwaves [36], lets us expect that a cylindrical beam shape allows for compressing materials inside the cylinder. A proof-of-principle has already been obtained in glass by Xie *et al*, with a single pulse shaped as a higher-order Bessel beam with circular polarization to generate a high-refractive index rod inside the bulk of glass [37].

Recent results have shown that zeroth-order Bessel beams induce, in a single shot, a very high energy density plasma [38], thanks to the process of resonance absorption [39], which occurs for polarization oriented perpendicular to the nano-plasma rod. With the aim of generating extreme states of matter, we have used a radially-polarized first-order Bessel beam, with a focal region shaped as a high-aspect ratio cylinder with an 800 nm diameter. Here, we report, for the first time to our knowledge, the generation of high aspect ratio nano-pillars vertically standing on the surface of sapphire. The positive structure is created by the high pressures generated below the material surface by ultrashort first-order Bessel pulse. Straight rods and wavy types of nano-pillars have been generated, with lengths up to 15 μm. We have identified a model to explain the three different regimes observed, that range from the extrusion of quasi-solid material to the jet of liquid material, where capillary instabilities are observable. We also investigate the role of pulse duration and polarization in the nano-pillar formation process.

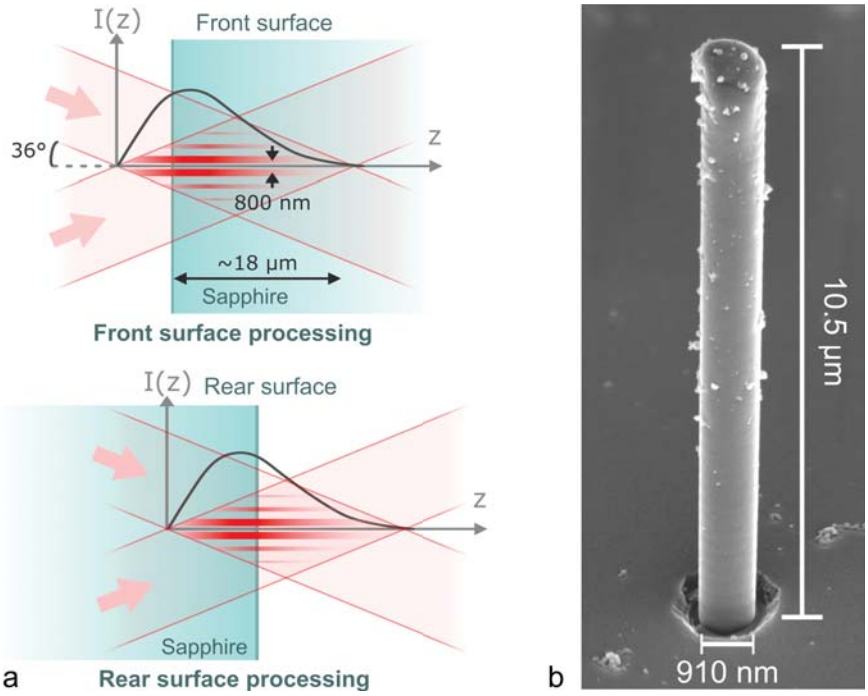

Figure 1: (a) Concept of the laser illumination strategy. A first-order, ultrafast Bessel beam is focused across the sample front or exit surface. The focal region is shaped as a hollow cylinder surrounded by several rings. The solid black line sketches the intensity of the cylinder along the propagation. In each configuration, the intensity is kept higher inside the bulk than on the surface. (b) Example of a nano-pillar produced after single shot illumination on the sample back surface, in radial polarization, 115 fs pulse duration.

2 Nano-pillars generation from the sapphire surface

Figure 1(a) shows a concept of our experiments. We studied the interaction of a radially or azimuthally polarized first-order Bessel beam crossing the front or the exit surface of a sapphire sample. The beam is produced from a primary femtosecond, linearly polarized zeroth-order Bessel beam [24] using a spatially variant half-waveplate. The beam cross-section features a doughnut-shaped focus, surrounded by several rings of lower intensity. The Bessel beam is characterized by a cone angle of 36° (equiv. numerical aperture 0.6), which imposes a doughnut diameter of about $800\,\mathrm{nm}$, which extends over a propagation length of about $20\,\mu\mathrm{m}$ (FWHM) in air, *i.e.,* $35\,\mu\mathrm{m}$ in sapphire. Technical details are provided in section Methods, and the experimental beam characterization is shown in Supplementary Figure S.1.

We first investigate focusing of the Bessel beam across the sample exit side, using $115\,\mathrm{fs}$ pulses, with energies ranging from $4.4\,\mu\mathrm{J}$ to $7\,\mu\mathrm{J}$ at the sample site. A representative outcome of the intense laser-matter interaction is depicted in Figure 1(b), demonstrating the generation of a high aspect ratio cylindrical nano-pillar from the surface. It has a diameter of $\sim 900\,\mathrm{nm}$ for a height exceeding $10\,\mu\mathrm{m}$. The primary objective of this paper is to elucidate the underlying mechanism responsible for the formation of this remarkable structure.

For each pulse energy, we have scanned the relative position of the surface within the beam by steps of $1\,\mu\mathrm{m}$. The fluence of the main Bessel ring, *i.e.*, the fluence on the tubular focus, varies smoothly along the propagation. It is shown as a solid line in Figure 1(a). Therefore, the fluence distribution in the material bulk varies at each step.

Figure 2 shows a series of Scanning Electron Microscopy (SEM) images of the nano-structures produced after single-shot irradiation, for a pulse energy of $6.1\,\mu\mathrm{J}$ at different positions in the beam, without further processing other than sample metallization for SEM imaging (see section Methods). We have characterized three different morphologies of high-aspect-ratio nano-pillars formed at the surface of the sapphire sample, which were ranked by the fluence at the sample surface. For the lowest fluences, we observe straight nano-pillars. In Figure 2(b), the diameter of the nano-pillar is $800\,\mathrm{nm}$ for a height of $4.4\,\mu\mathrm{m}$. Its surface shows a slight periodic corrugation, on which we will comment in the next section. At higher fluence, the second regime is featured by a slick surface and often small perturbations of the nano-pillar shape at the top of the structure. In this regime, we found a maximal pillar height of $13\,\mu\mathrm{m}$ with a typical diameter of $700\,\mathrm{nm}$, leading to an aspect ratio of 21. The first two regimes are highly reproducible from shot to shot. At the highest surface fluences, the third regime presents nano-pillars with highly wavy structures. This regime is nearly stochastic. Figures 2(g-i) show three different structures obtained in close conditions. Above this regime, only nano-droplets can be found at the sample's surface, tens of micrometers away from the small crater, similarly as in Figure 2(g).

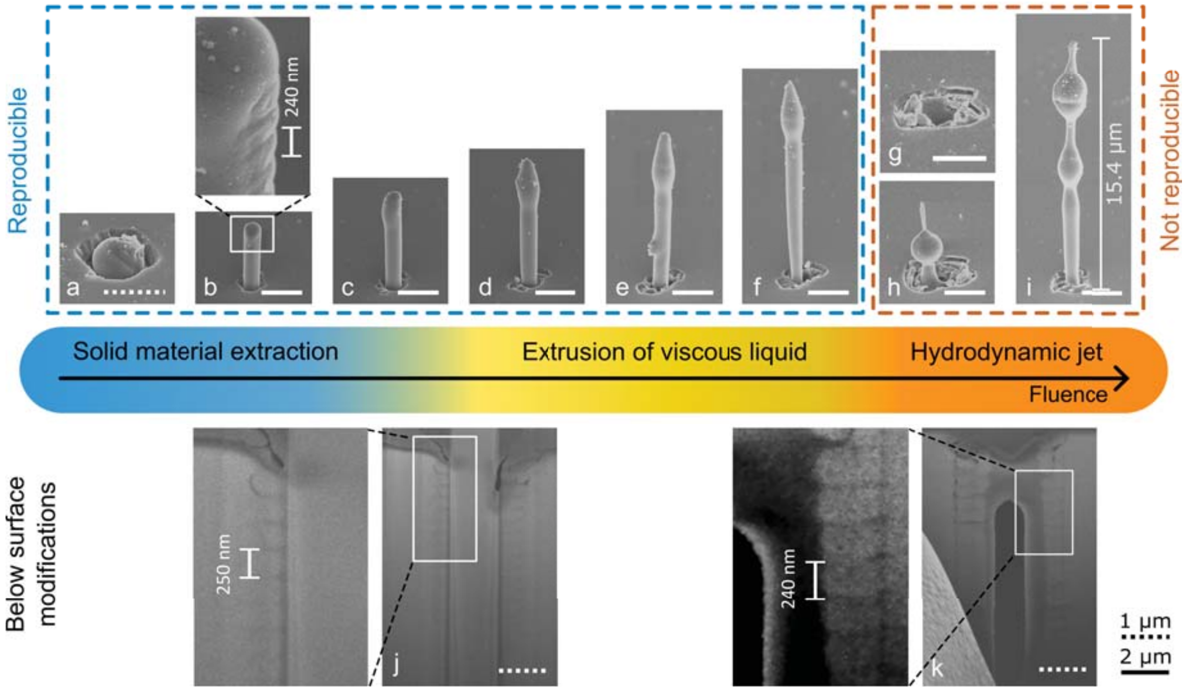

Figure 2: Evolution of the nano-pillar morphology depending on the main Bessel ring fluence. We used pulses with pulse duration of $115\,\mathrm{fs}$, energy of $6.1\,\mu\mathrm{J}$, and different relative positions beam-sample. We can identify three different regimes depending on the beam fluence. In the case of the first and second regimes, the nano-pillars are reproducible (refer to Methods for the reproducibility), while for higher fluence, the nano-pillars are no more reproducible from shot to shot. At the bottom of the figure, we show the modifications produced below the surface (see Methods for more details). We also insert some close-ups to show smaller details. Scale bars are $2\,\mu\mathrm{m}$ for the solid ones and $1\,\mu\mathrm{m}$ for the dashed ones.

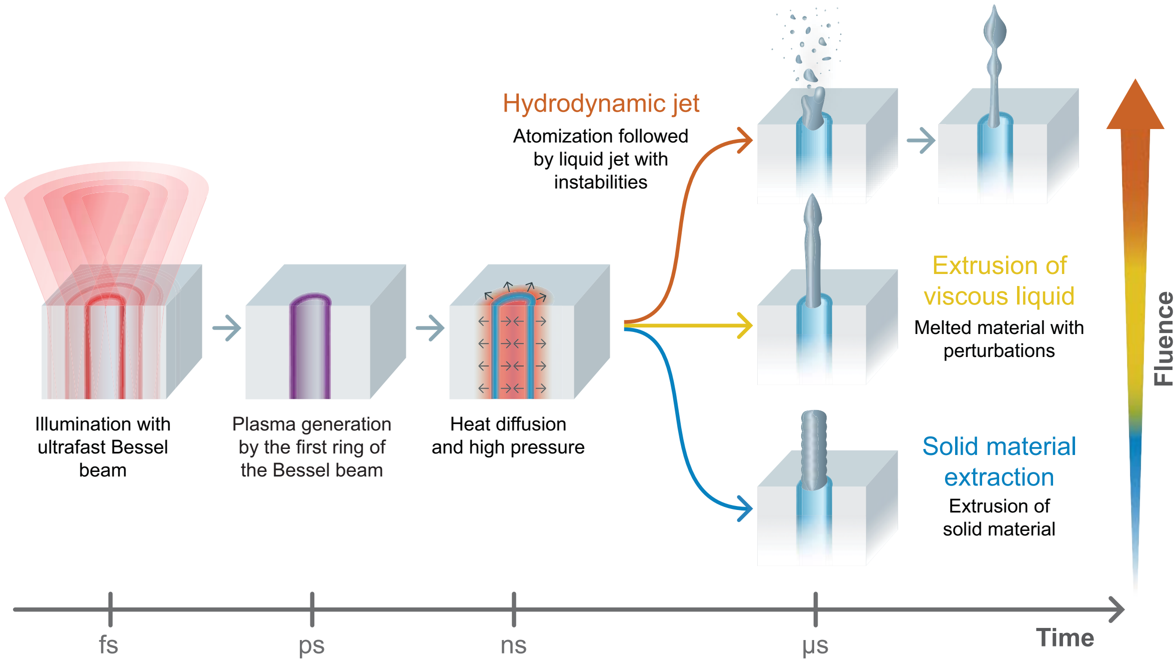

Figure 3: Concept of the nano-pillar formation mechanism for the three different regimes that can be controlled via the fluence. The process is identical if the laser pulse propagates from top to bottom or vice-versa.The timescales are estimated orders of magnitude from the literature [26,40].

3 Formation mechanism of the nano-pillars

Here, we propose a model explaining the different nano-pillar formation regimes. We expect that the pulse propagation remains quasi-linear because of the high cone angle used. Therefore, the main ring of the radially-polarized Bessel beam generates a plasma distribution shaped like a high aspect ratio nano-tube (see Figure 3) [34]. The pressure and temperature on the tube increase sharply, potentially up to the warm dense matter regime [38,41]. This leads to radial forces toward the tube center and outward, as in the case of surface excitation by an optical vortex [42]. In our case, a long column of material is pressurized, and the relaxation involves material transfer from bulk across the surface. We notice that, in our conditions, the beam fluence is higher in the sapphire bulk than on the surface. It is probable that material is ejected because the pressure deep in the material bulk is higher than close to the surface. Similar high-pressure conditions were observed for zero-order Bessel beam, leading to the generation of nano-spheroid on YAG [43] and in nano-channel formation with the so-called surface assisted material ejection [44].

Depending on the laser-deposited energy, the material at the center of the tube core can be in different physical states. As highlighted before, the three regimes we have identified depend on the fluence at the exit surface. This is obviously related to the energy deposition in the material close to the surface. Supposing that a higher fluence leads to a higher temperature in the material and to a material with lower viscosity and surface tension, we can understand the first regime as the translation of solid material, the second as the extrusion of high-viscosity fluid, and the third regime as the emission of low-viscosity liquid jet undergoing capillary instabilities. A concept figure with the stages of the nano-pillar generation is shown in Figure 3, and we comment on each regime in more detail in the paragraphs below.

First regime: translation of rod-shaped solid material The first regime presents very regular nano-pillars and almost negligible effects of the beam around the nano-pillar base (in Figure 2(a-c) note the limited damage on the surface). We suppose that the main ring of the Bessel beam creates a thin cylindrical layer of liquid material while the internal rod of material remains solid due to the low fluence. The layer of liquid material and the high internal pressure allow the translation of the rod outside the bulk. It is possible that higher fluence, deeper into the bulk, creates higher pressure conditions, leading to the propulsion of a solid nano-rod out of the sapphire bulk. This first regime appears for fluences between 0 and 2 (a.u.) (All arbitrary unit fluences across the different figures are expressed using the same reference).

The translation mechanism is confirmed twofold. First, we remark on the presence of periodic nanostructures on the surface of the nano-pillars (see the horizontal lines in the close-ups of Figure 2[b],[j], and [k]). They match very well the pattern observed in the material bulk, observed after Focused Ion Beam (FIB) milling below the nano-pillars (bottom row in Figure 2). This clearly indicates that the material remains solid during the transformation and maintains the structures created beforehand. We note that the period of the horizontal nanostructures remains constant among the different parameters for which they are observed. These structures are attributed to highly localized material amorphization by an interference pattern between the onset of the Bessel pulse reflected on the exit surface and the trailing part of the Bessel beam. A simulation of the resulting intensity distribution is shown in Supplementary Figure S.2. This interference has a period of $\frac{\lambda}{2n\cos\theta} = 241$ nm, where λ is the central wavelength, n is the sapphire refractive index, and θ the Bessel beam cone angle in the medium, which is in excellent agreement with the experimental value of about $240\,\mathrm{nm}$. In this framework, the periodic pattern is inscribed before material ejection.

Second, we performed transmission electron microscopy (TEM) in Bright Field mode (BF) in addition to FIB investigations. The BF-TEM observations of the nano-pillar in Figure 2 (b) is shown in Figure 4. The BF-TEM image (a) of a thin foil of the pillar and part of the bulk material show Bragg diffraction contrasts (dark lines) proving that both pillar and bulk sapphire are crystalline. Moreover, the close-up (b) and the associated selected area electron diffraction (SAED) pattern (c) performed in one zone axis ([3-2-2]) confirm that the pillar is a mono-crystal (c), as the initial sample material. In (a), the dark lines around the pillar, below the surface (see dashed ellipse), are characteristic of highly stressed material. They become denser when getting closer to the position of the cylindrical focus, *i.e.* around the translated nano-rod. The periodic gray triangles (solid arrows), with a typical size of $50\,\mathrm{nm}$ observable below the surface around the nano-rod, are amorphous zones. Amorphization has been induced by the different phase transitions and fast cooling. The fact that the pillar is effectively a mono-crystal shows that it has not undergone any phase transition. In fact, the fast cooling of a liquid would result in a

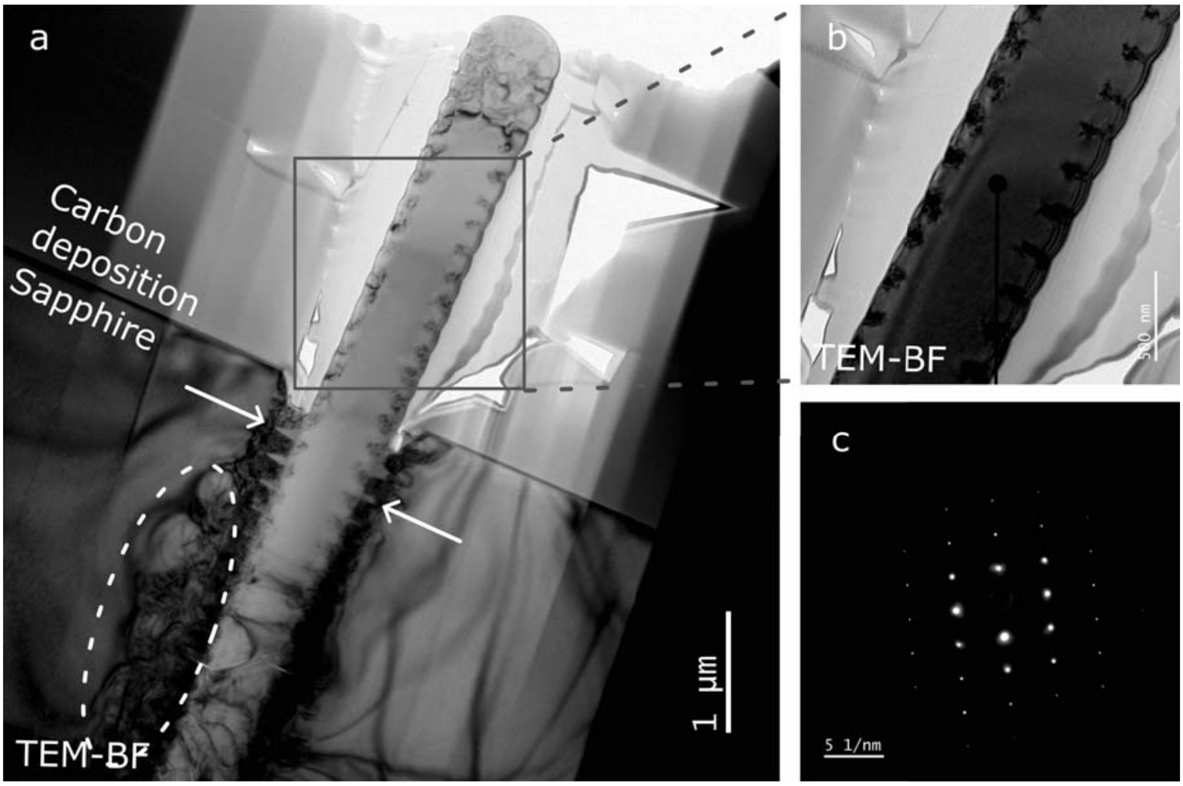

Figure 4: Transmission electron microscope (TEM) images of the nano-pillar shown in Figure 2 (b). Bright Field TEM (BF-TEM) image (a) shows a thin foil with the complete pillar and part of the bulk. The material on both sides of the pillar is a protection layer of carbon; its deposition is necessary for the FIB preparation. The close-up of the pillar (b) and its selected area electron diffraction (SAED) pattern observed along [3-2-2] zone axis (c) highlight the crystalline state of the pillar.

polycrystalline material, and not a well-formed monocrystal. Therefore, the nano-pillar generation is due to a translation of the rod from the material's bulk.

The nanopillar height varies both with the pulse energy and position of the beam inside the sample. As we will detail in section 4, we have observed that the fluence reached on the sample surface is the most discriminatory parameter. We show in Figure 5 the evolution of the height of the nano-pillars as a function of the fluence on the sample surface. In the first regime, the nano-pillar height varies linearly with the fluence. The maximum height reached in the first regime is also linked to the Bessel beam length inside the medium, which is typically $18\,\mu\mathrm{m}$ (the effective insertion is shown in detail in supplementary material, Figures S.3 to S.5). We note that in this regime, as in the second, we did not observe a void below the nano-pillars. Either the material density has been highly depressed over a significant volume (note that sapphire density varies by about 25% between the solid and the molten states [45]), or a void is present but below the maximal depth reached by FIB milling, *i.e.,* $\sim 10\,\mu\mathrm{m}$.

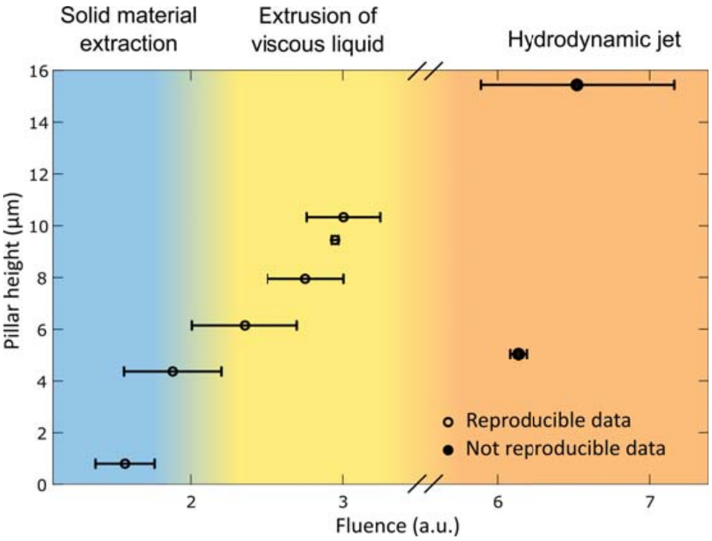

Figure 5: Height of the nano-pillars as a function of the main Bessel ring fluence on the exit surface for pulses with pulse duration of $115\,\mathrm{fs}$, energy of $6.1\,\mu\mathrm{J}$. The fluence is determined by the relative beam-sample position. The data corresponds to the nano-pillars shown in Figure 2.

Second regime: reproducible nano-pillars with slick surface The nano-pillars of the second regime (Figure 2[c-f]), for fluences in the range of typically 2 to 3.5 a.u., present a slick surface: they do not show transverse periodic patterns. Most of the structures also present small perturbations at their extremities. We understand this regime as the extrusion of highly viscous liquid sapphire through the nozzle formed by the surface crater upon laser impact. We can notice that the structures produced in this regime have a smaller and smaller diameter from top to bottom: this can be explained by the progressive closing of the surface aperture because of simultaneous cooling during the extrusion. The small perturbations at the extremities can be due to the reshaping of the extruded rod because of internal stresses produced by temperature inhomogeneities. In this regime, since the surface of the pillar is molten, the periodic pattern vanishes.

We see in Figure 5, that in this regime, the nano-pillar height increases approximately linearly with the surface fluence as in the case of the first regime. It reaches a maximal value of $\sim 13\,\mu\mathrm{m}$ in the second. (Note that the error bars along the fluence axis are large because the fluence profile of the Bessel beam is steep in some regions. For this reason, the $\pm\ 1\,\mu\mathrm{m}$ error on the sample-beam position can transfer to large error bars on the fluence).

Jets with capillary instabilities Before detailing the third regime, we briefly recall literature results on capillary instabilities as they are characteristic of this regime. Capillary instabilities are due to the fact that the surface energy of a cylindrical jet is not the minimum. Therefore, any perturbation tends to break the jet into segments or droplets as observed early by Plateau and Rayleigh [46]. Capillary perturbations on jets of molten material were observed in previous laser-based processes, as in laser-induced nano-jetting from metallic films [47,48] and in vortex beam machining of silicon [49]. The theory that describes the

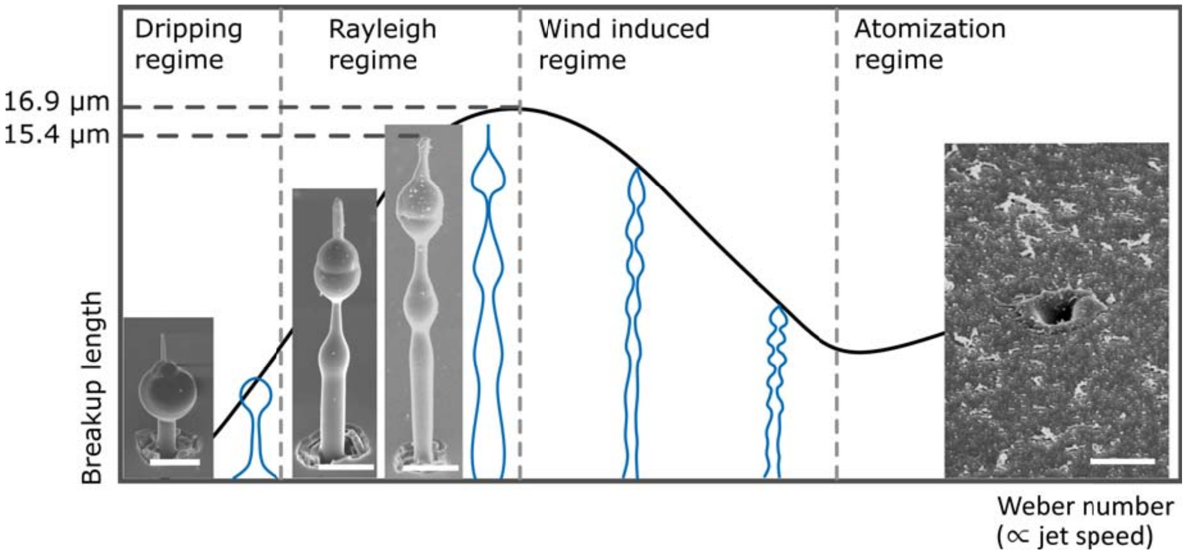

Figure 6: Evolution of the breakup length versus the jet speed or the Weber number (We) from the capillary instability theory, highlighting the different regimes [46]. The blue shapes are profiles of real water jets in the three regimes (not in scale) [50,51]. The SEM images show examples of nano-pillars produced in the third regime, highlighting the high degree of correspondence between the two cases. Scale bars: $2\,\mu\mathrm{m}$.

behavior of liquid jets has been initially developed by Rayleigh and Plateau and was further completed as capillary instability theory [50]. It distinguishes different regimes depending on the Weber number or the jet speed (see Figure 6). The Weber number is defined as $\mathrm{We} = \rho v^2 d/\sigma$, where ρ is the density of the fluid, v is the jet speed, d is the jet diameter, and σ is the surface tension of the liquid.

In Figure 6, we show with solid blue lines the typical morphology of water jets for different jet speeds and Weber numbers from references [50,51]. At low Weber numbers, the jets are cylindrically symmetric (dripping and Rayleigh regimes). Increasing the Weber number, the jet starts to be asymmetric (winded regime) and eventually reaches the atomization regime, where the jet sprays into particles much smaller than the nozzle diameter. (Dripping and Rayleigh regimes can easily be observed, for instance, in the coffee jet of an espresso machine.) In the same figure, the black solid line shows the evolution of the breakup length, for which the jet breaks into separate droplets [46].

The Weber number shows that the temperature of the material greatly affects the regime of the jet. In the liquid phase, dielectric materials undergo an extreme drop in viscosity and surface tension by orders of magnitude with temperature increase [52]. In our case, we assume that a higher fluence leads to a higher temperature, hence higher jet speed, lower viscosity, and lower surface tension, therefore corresponding to a higher Weber number.

Third regime: wavy nano-pillars The third regime corresponds to the nano-pillars shown in Figure 2(g-i). This regime is nearly stochastic and appears for fluences above 3.5 (a.u.). As a consequence of the extremely high sensitivity to processing parameters, the shot-to-shot reproducibility varies between 0 and approximately 70 %. In this regime, we can observe either the absence of any kind of structures except a crater (Figure 2[g]), or the presence of a small structure (Figure 2[h]), or even very high nano-pillars reaching $15\,\mu\mathrm{m}$ in height (see Figure 2[i]). All the pillars in this regime present very wavy morphology compared to the previous regimes. The comparison of their morphology with water jets is striking as shown in Figure 6. The dripping regime shape corresponds to the small pillar shown in Figure 2(h). This nano-pillar presents an elongated filament at the top, a sign of a probable generation of satellite droplets before solidification [53]. The nano-pillar in Figure 2(i) can easily be associated with the Rayleigh regime.

To explain the third regime, we suppose that, at high fluences, the material inside the excited tube of material is in the liquid phase, with low viscosity, low surface tension, and under higher temperature and pressure than in the previous regimes [54]. This condition leads to a more explosive ejection than in the other regimes, as suggested by the more significant cracks on the surface, which are much wider than the nano-pillar diameters (see the surfaces in Figure 2[g-i]). These conditions correspond to the hydrodynamics of liquid jets which undergo capillary instability as described above. Therefore, we understand our results with the following scenario: after material excitation and heating, an explosive phase occurs within the atomization regime. This phase is followed by the emission of a jet at a lower Weber number. The jet is perturbed by instabilities and then re-solidifies. The first explosive phase is probably the cause of the stochastic behavior in the third regime. The explosion can indeed easily modify the aperture on the surface, which plays the role of a nozzle, with obvious influence on the regime of the jet [55]. We also remark that FIB milling reveals a void underneath the nano-pillar (Figure 2[k]), highlighting the extreme thermodynamics at play in this regime.

In the jet breakup theory, it is possible to calculate the wavelength of the main instability mode [56]. This length depends on the physical parameters of the sapphire. In our case, the calculated wavelength has a maximum at $\lambda = \pi d\sqrt{2 + 6\sqrt{\frac{\rho\nu^2}{2d\sigma}}} \approx 6\,\mu\mathrm{m}$, where d is the jet diameter ($700\,\mathrm{nm}$), ρ the density ($3030\,\mathrm{kg\,m^{-3}}$), ν the kinematic viscosity ($1.8 \times 10^{-5}\,\mathrm{m^2\,s^{-1}}$), and σ the surface tension ($0.67\,\mathrm{N\,m^{-1}}$), where this data correspond to liquid sapphire at its melting temperature of $2323\,\mathrm{K}$ [45,53]. It fits remarkably well with the period of $5\,\mu\mathrm{m}$ observed in Figure 2(i).

We also remark that among all the results obtained, including those presented in subsequent sections, a maximal nano-pillar height of about $15\,\mu\mathrm{m}$ has been reached many times in highly different conditions (energy, pulse duration, polarization, beam-sample relative position). This highlights the universality of the jetting process in the third regime again, as described by the capillary instability theory, which predicts a maximum of the breakup length, as we showed in Figure 6. The breakup length is the length over which the jet remains within a single segment of fluid. Above this maximal distance, the jet breaks up into droplets. The maximum height we found experimentally fits extremely well the theoretical formula of the breakup length $L = 0.5\, d\sqrt{\frac{\rho}{\rho_a}} = 16.9\,\mu\mathrm{m}$, where ρ_a is the density of air in our case [57].

Since the maximal breakup length corresponds to the transition between capillary and shear instability ($\mathrm{We} \approx \rho/\rho_a$ [57]), we can estimate that the maximum jet speed is of about $800\,\mathrm{m\,s^{-1}}$ within the same order of magnitude as shadowgraphy measurements of laser-induced forward transfer [58].

We also highlight that the cooling process is extremely fast since, in our experiment, the laser beam and the liquid sapphire jets are horizontal. We did not observe significant titling of the nano-pillars that could be attributed to gravity.

4 Influence of the processing parameters

In this section, we investigate the impact of the different processing parameters on the nano-pillar formation.

Fluence on the sample surface In this subsection, we show that the nano-pillar formation process is mostly determined by the fluence of the main ring (doughnut) of the Bessel beam on the sample surface. In Supplementary Figure S.3, we plot the evolution of the beam fluence of the main Bessel ring as a function of distance, and we have indicated the positions at which a nano-structure has emerged on the surface, for a fixed pulse energy of $6.1\,\mu\mathrm{J}$, together with the corresponding SEM images. It is apparent that for different positions, nano-pillars belonging to the three regimes mentioned above have emerged. We have repeated the experiment for different energies, and we have summarized our results in Supplementary Figure S.6, where we report the height (top panel) and maximum diameter (lower panel) of the repeatable nanostructures (first and second regime) as a function of the main Bessel ring fluence on the sample exit surface. In the top panel, we also show the corresponding SEM pictures. The color marks the pulse energy.

We observe that the nano-structure average diameter remains nearly constant throughout our experiments, ranging from $800\,\mathrm{nm}$ to $\sim 1.2\,\mu\mathrm{m}$. Besides, the height evolves quasi-linearly with the fluence. Most importantly, we can distinguish that the morphology of the nano-pillars changes for a fluence of $\sim$ 1.7 (a.u). The third regime, with much less reproducibility, is reached for a fluence above 3.5 (a.u).

As we will see below, similar nano-pillars could be obtained for different processing conditions: azimuthal polarization, front surface processing, and pulse durations, for which we have repeated the same analysis (see next sections and supplementary figures S.4 to S.10). The pulse energy and the position of the beam with respect to the surface both modify the deposited energy distribution and, therefore, the nano-pillar formation. Importantly, we remark in our data that the fluence of the main Bessel ring on the processed surface, shown in the horizontal axis in these figures, allows for distinguishing the regimes among the different pulse energies and positions used. It is, therefore, the important effective control parameter allowing us to classify our results. We can also see that the fluences corresponding to transitions are relatively close among the different pulse durations. These remarks hold for nearly all cases except for high pulse energy or long pulse duration. We identify the regimes using the SEM images and represent them using the colorbar between the two panels in each figure.

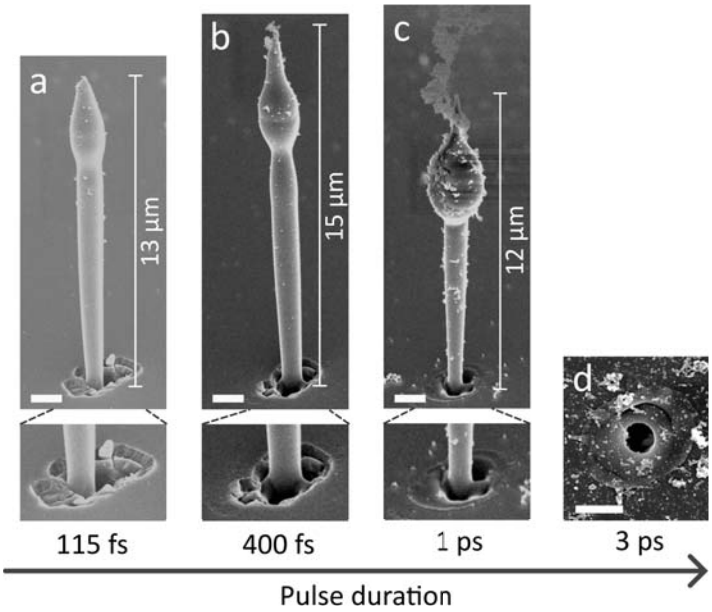

Figure 7: SEM images of laser-generated structures for different pulse durations. Figures a to c with pulse energy of $6.1\,\mu\mathrm{J}$ and d with a lower pulse energy of $5.3\,\mu\mathrm{J}$. Scale bars are $1\,\mu\mathrm{m}$.

Pulse duration Pulse duration is an important parameter for the laser processing of dielectric materials. We compared four pulse widths ($115\,\mathrm{fs}$, $400\,\mathrm{fs}$, $1\,\mathrm{ps}$, and $3\,\mathrm{ps}$). In the configurations we explored, we could obtain nano-pillars in each case except for $3\,\mathrm{ps}$. The examples of the laser-generated structures are presented in Figure 7 for a pulse energy of $6.1\,\mu\mathrm{J}$ (a-c) and $5.3\,\mu\mathrm{J}$ (d). Increasing the pulse duration in the picosecond regime leads to nano-structures that apparently have all undergone transient liquefaction, corresponding to an absence of the first regime (we note that straight nano-pillars of the first regime were observed for 400 fs pulse duration). Stronger thermal effects are also apparent when examining the close-ups of Figure 7 (bottom row): at lower pulse duration (a-b), the crater at the surface is dominated by cracks while longer pulse duration (c-d) features molten material around the nano-pillar base. In most of the images, we also notice the strong presence of small particles around and on the nano-pillars when increasing the pulse duration.

In particular, the case at $1\,\mathrm{ps}$ presents a structure at the top of the nano-pillars that very well matches the images of a jet of a molten metallic alloy in a liquid coolant in the atomization regime of reference [59]. Our results for longer pulse durations can be understood as resulting from a first step of atomization followed by a jetting regime after the release of material through the surface and subsequent jet speed reduction. We note that the third regime with picosecond pulse durations is qualitatively less critical on position parameters than in the case of femtosecond pulse durations. We explain the overall differences between pulse durations as originating from lower pressure and temperature gradients for long pulse durations.

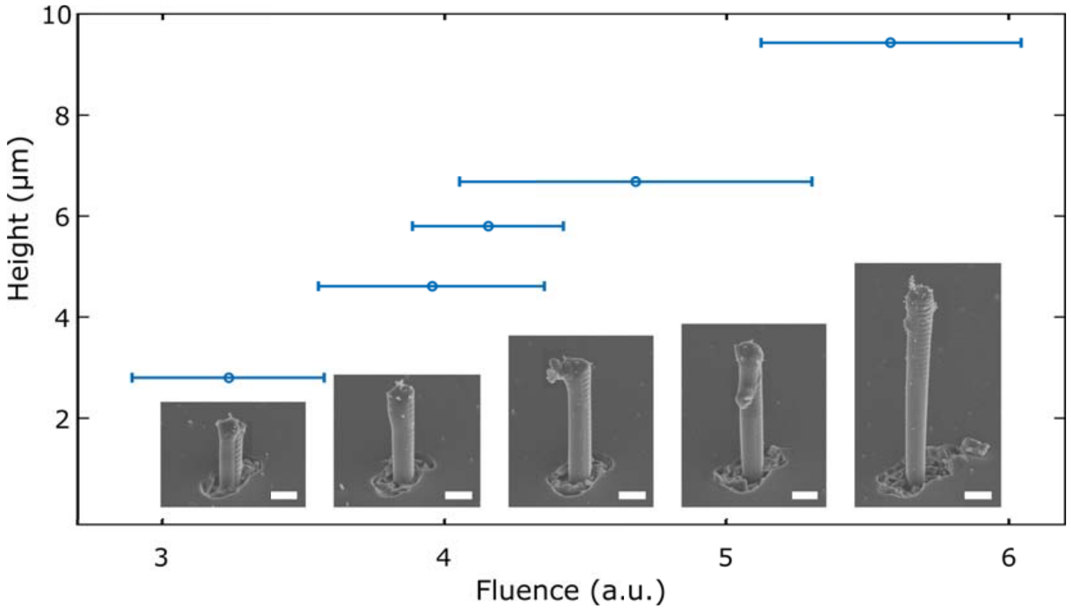

Figure 8: SEM images of nano-pillars obtained with azimuthal polarization with a pulse energy of 6.1 µJ. The graph shows the height as a function of the main Bessel ring fluence on the exit surface. Scale bars are 1 µm.

Polarization As mentioned in the introduction, radial polarization highly enhances laser absorption via the resonance absorption mechanism. We repeated our experiments by switching the polarization state to azimuthal while maintaining all other parameters identical. A representative selection of results is shown in Figure 8. With the azimuthal polarization, even at high fluence, the nano-pillars remain straight and present the same periodic interference pattern as observed in Figure 2(b), in the first regime. The highest nano-pillar we obtained is 9 µm high and 0.9 µm in diameter, leading to an aspect ratio of 10. We remark that the diameter of the nano-structures remains similar as in the case of radial polarization. As shown in Figure 8, the nano-pillar height evolves quasi-linearly with fluence, with a slope reduced by a factor 2 compared to the radial polarization. Our results highlight the difference in energy density deposition between radial and azimuthal polarizations: they show that the material irradiated with radial polarization reaches a higher temperature due to the resonance absorption [60], as it is the case in numerical simulations of laser-surface interaction with Gaussian beams [61].

Front surface processing We have also investigated the possibility of producing nano-pillars from the sapphire front surface. The tail of the beam was inserted in the sample, reproducing with symmetry the exit surface configuration (see Figure 1). Nano-pillars produced with radial polarization and pulse duration of 115 fs are shown in Figure 9. We show the highest pillar obtained across the different sample positions for each pulse energy. The morphology of the nano-pillars is consistent with the mechanism described above. For the lower energies, the nano-pillars are straight, and the height reaches 8 µm for an aspect ratio of 9 (diameter: 0.9 µm). We note that even at low fluence, the nano-pillars do not present the periodic pattern that we observed previously on the exit surface configurations: this supports the

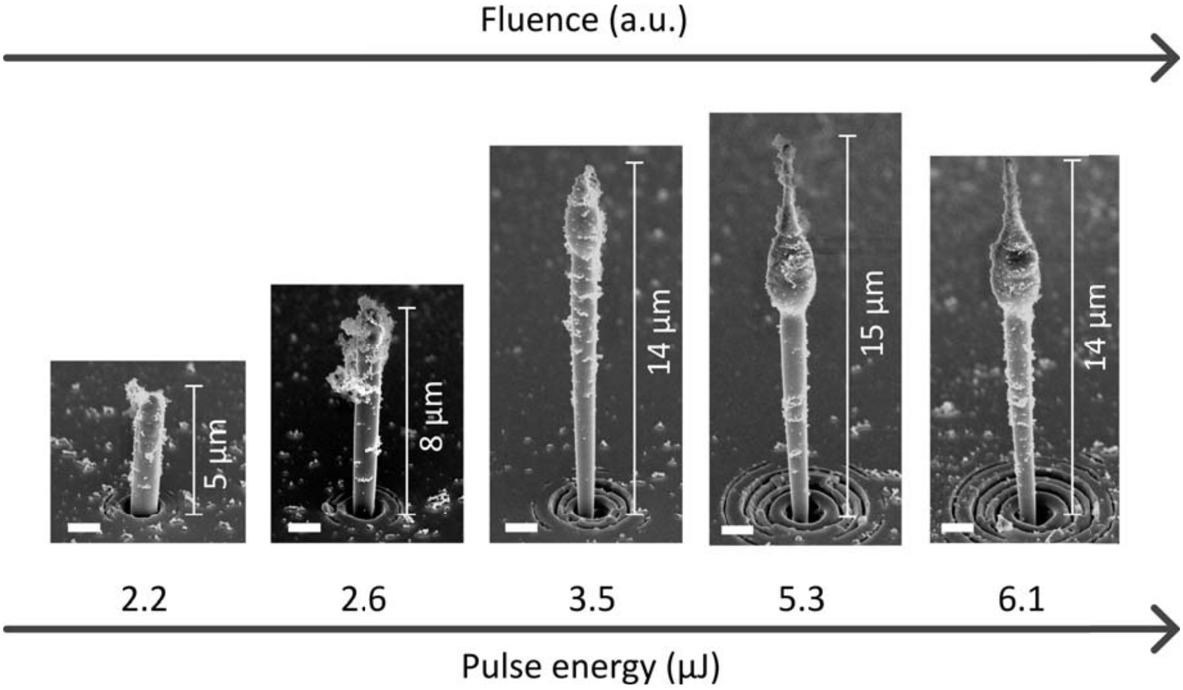

Figure 9: SEM images of the highest nano-pillars generated with front surface processing at different pulse energies and $115\,\mathrm{fs}$ pulses. Scale bars are $1\,\mu\mathrm{m}$.

explanation of the interference between the beam and its reflection since it is not possible on the front surface configuration. At higher fluence, the capillary perturbations appear again, and the maximum height of nano-pillars observed is $15\,\mu\mathrm{m}$, again in excellent agreement with the value predicted by the jet breakup theory (see section Third regime: wavy nano-pillars). We can note the high presence of small particles that can be attributed to the surface damages caused by the outer rings of the Bessel beam and the probable occurrence of the atomization regime preceding nano-pillar formation.

Array fabrication Nano-pillars hold significant relevance across various domains. Solar cells benefit from the incorporation of nano-pillars to enhance light absorption [62,63]. In biology, nano-pillars find utility in areas such as cell adhesion studies and tissue engineering, facilitating interactions between cells and artificial substrates [64,65]. Moreover, in the realm of quantum electrodynamics, nano-pillars play a pivotal role in the manipulation of light-matter interactions, enabling the exploration of quantum phenomena [66]. Additionally, nano-pillars find application as resonators, contributing to the development of highly efficient optical and electronic devices [67].

We have produced, as a proof-of-principle, periodic arrays of nano-pillars produced by sequential positioning and single-shot illumination. We believe that parallel processing could be identically performed. An example is shown in Figure 10. The minimal spacing for which the nano-pillars are

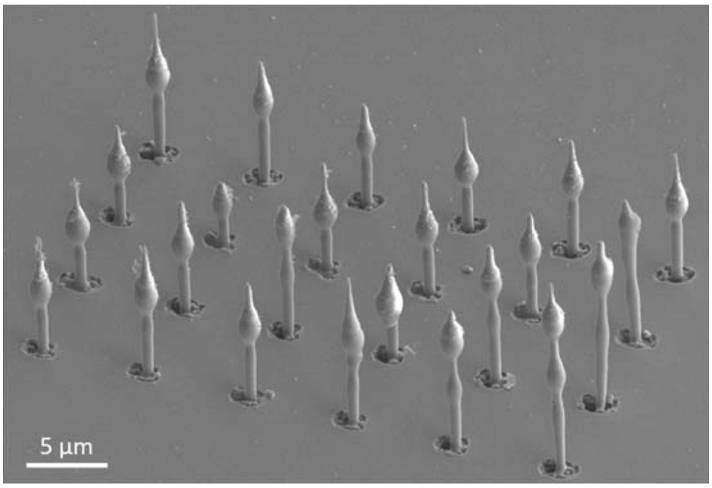

Figure 10: SEM picture of a matrix of nano-pillars with spacing of 7 µm (energy 6.1 µJ, pulse duration 115 fs and radial polarization).

homogeneous among the array is 7 µm. We remark it corresponds to the minimum separation distance for which an optical ray of the Bessel beam reaching the surface is blocked by a previously-inscribed 20 µm deep modification. We can therefore deduce that strong modifications are present deep within the bulk material underneath the nano-pillars.

5 Conclusion

We demonstrated for the first time the possibility of generating nano-pillars atop sapphire surface using a radially or azimuthally polarized first-order Bessel beam with a single ultrafast laser pulse. The nanostructures reach a height up to 15 µm with sub-micrometer diameter. Several morphologies could be observed with three main regimes. In a first approximation, the regimes can be controlled by the fluence of the Bessel beam on the exit surface. For the lowest fluences, straight nano-pillars are formed by the translation of solid material from the bulk. In the second regime, slick nano-pillars are formed by the extrusion of highly viscous molten sapphire. In the third regime, several morphologies of wavy nano-pillars could be observed and interpreted in the framework of the capillary instability theory of liquid jets of low viscosity. This theoretical framework very well predicts the period of the oscillations along the nano-pillar height, as well as the maximal nano-pillar height itself. Its universality has been observed among all the results we obtained with highly different laser pulse configurations.

Increasing the pulse duration reduces spatial gradients of temperature. Laser pulses with picosecond duration produce more thermally affected material while suppressing the first regime in which straight nano-pillars can be generated. The azimuthal polarization, for which the absorption is less intense, leads to less explosive conditions and favors this first regime.

Preliminary results, not reported here, show that similar results could be obtained within MgO crystal. They also indicate that the evolution of the fluence distribution along the beam propagation is highly influential in controlling the process: spatial distribution of laser-deposited energy density plays a key role in the mechanism of the nano-pillar formation. More studies are needed to fully decipher it. Specifically, next research should focus on evaluating the deposited energy density gradients and thermodynamic conditions to enable modeling of the overall nano-pillar generation process. Finally, we succeeded in producing matrices of nano-pillars with $7\,\mu\mathrm{m}$ pitch. The main benefits of this nanofabrication approach are its speed, absence of pre- or post-processing, and that it does not require clean-room facility. Our results open new perspectives in the field of laser-matter interaction and new material phase synthesis by compression. This fast nano-pillar fabrication approach will enable new applications in a number of different fields, such as metamaterials, mechanical components, nano-photonics, nano-phononics, or sensing.

6 Methods

6.0.1 Experimental setup

We used a Ti:Sapphire laser with central wavelength at $800\,\mathrm{nm}$. Thanks to a Spatial Light Modulator and a 2f-2f system (relay lens and microscope objective Olympus MPLFLN x50), we obtained a Bessel beam with a cone angle of $36°$ in air at the sample position. To obtain a radial or azimuthal polarization, we inserted a radial polarizer converter (ARCoptix, Switzerland) between the first lens and the microscope objective of the demagnification system. Because of the phase singularity imposed by the radial or azimuthal polarization distribution, the zero-order Bessel beam is transformed into a first-order one.

To observe both sample and beam, we used a 2f-2f system composed of a microscope objective (Olympus MPLFLN x50) and a relay lens to have the imaging on a camera (Stingray F146B with 14 bits).

6.0.2 Beam shape

The obtained Bessel beam was featured by a length in air of about $20\,\mu\mathrm{m}$ (FWHM) and an angle of $36°$, leading to a central ring of about $800\,\mathrm{nm}$ diameter (considering the intensity maxima). Because of a singularity of the radial polarizer converter, a drop in the intensity profile was generated in the middle of the beam (see for the beam profile in Figure S.1). The pulse duration was checked using the autocorrelator PulseCheck 50 (APE, Germany) before the spatial light modulator. The dispersion induced by the rest of the optical setup is quasi-negligible.

6.0.3 Sample

The samples are sapphire c-cut with thickness $150\,\mu\mathrm{m}$. In our experiment, the sample is mounted on a precision 3-axis translation stage to allow the machining at different beam-sample positions. The sample was set on a motorized kinematic mount to ensure its orthogonality to the beam direction.

6.0.4 Experimental procedure

We scanned the relative beam-sample position over $30\,\mu\mathrm{m}$ around the peak of the beam by steps of $1\,\mu\mathrm{m}$. After the characterization of the beam and the alignment of the sample, we repeated six shots for each set of parameters with a distance of $25\,\mu\mathrm{m}$ between two consecutive shots. We consider that the regime is repeatable if at least five shots over six produce the same nano-pillar morphology within a height fluctuation of $\pm 1\,\mu\mathrm{m}$. We remark that it is possible that some nano-pillars could have been broken due to the sample handling between processing and SEM imaging, as we found nano-pillar-shaped structures on the surface of the sample.

6.0.5 Procedure for in-bulk SEM images

To obtain the images of the modifications inside the materials (see Figure 2), we milled the region around the laser damage with a focused ion beam (FEI Helios 600i). To avoid charging effects, we deposited a layer of Chromium of about $20\,\mathrm{nm}$ to $25\,\mathrm{nm}$. To protect the interesting area from the direct interaction with the ion beam, we deposited a layer of $1\,\mu\mathrm{m}$ of platinum above. We performed a milling procedure with a nominal depth of $15\,\mu\mathrm{m}$ at a current of $21\,\mathrm{nA}$ to create a cuvette offering SEM imaging access, positioned about $3\,\mu\mathrm{m}$ from the laser damage. In a second step, we performed two cleaning cross-sections: at $9\,\mathrm{nA}$ to approach the damage and subsequently at $2.5\,\mathrm{nA}$ to produce clean sections of the modified region. All the images were taken with an angle of 52° from the vertical.

6.0.6 Procedure for TEM images

The TEM foils were prepared using a Thermo Fisher Scientific FEI 125 Helios Nanolab 600i Focused Ion Beam (FIB). The nano-pillar was protected with a thick carbon coating (Figure 4 [a]) deposited on both sides and above the pillar before the milling and extraction of the foil. TEM characterizations were performed with a Cs-corrected TEM (NeoARM200F Cold FEG) operated at 200kV. The instrument is equipped with a wide-angle energy dispersive X-ray (EDX) spectrometer SDD CENTURIO-X from JEOL, two scanning transmission electron microscope (STEM) detectors (annular dark field and annular bright field from JEOL and Gatan) with a CMOS camera Gatan Rio (4kx4k), a CCD camera Ultrascan from Gatan (2kx2k), and an electron energy-loss spectrometer (EELS, Gatan GIF Quantum ER).

Supporting Information

Supporting Information is available from the Wiley Online Library or from the author.

Funding

This project has received funding from H2020 European Research Council (ERC) under grant agreement 682032-PULSAR, the European Union's Horizon 2020 research and innovation program under grant agreement No 825246 kW-flexiburst, the French Agence Nationale de la Recherche, projects DENSE (ANR-21-CE08-0005) and EQUIPEX+ SMARTLIGHT platform (ANR-21-ESRE-0040), and the EIPHI Graduate School (ANR-17-EURE-0002). This work was partially supported by the French Renatech network.

Author contributions

V.V.B, M.H., R.G., L. F. and F.C. developed the setup, V.V.B. performed most of the data acquisition with the help of M.H, V.V.B performed SEM imaging, V.V.B. and F.C. analyzed the experimental data. V.V.B. proposed the model, S.S.J. prepared the sample for TEM measurements, A.M.S.G. performed and interpreted TEM measurements. The manuscript was jointly written by V.V.B. and F.C. and revised by all authors.

Acknowledgments

Technical assistance by E. Dordor, M. Raschetti, R. Salut and C. Billet is gratefully acknowledged. AMSG and SSJ thank the consortium Lyon Saint Etienne de Microscopies and MANUTECH USD for the access to the TEM and FIB facilities respectively.

Conflict of interest

The authors declare no competing interests.

References

1. Kammel, R. *et al.* Enhancing precision in fs-laser material processing by simultaneous spatial and temporal focusing. *Light: Science & Applications* **3**, e169 (2014).

2. Manousidaki, M., Papazoglou, D. G., Farsari, M. & Tzortzakis, S. Abruptly autofocusing beams enable advanced multiscale photo-polymerization. *Optica* **3**, 525–530 (2016).

3. Jiang, L., Wang, A. D., Li, B., Cui, T. H. & Lu, Y. F. Electrons dynamics control by shaping femtosecond laser pulses in micro/nanofabrication: Modeling, method, measurement and application. *Light: Science & Applications* **7**, 17134 (2018).

4. Malinauskas, M. *et al.* Ultrafast laser processing of materials: From science to industry. *Light: Science & Applications* **5**, e16133 (2016).

5. Salter, P. S. & Booth, M. J. Adaptive optics in laser processing. *Light: Science & Applications* **8**, 110 (2019).

6. Teubner, U., Bergmann, J., van Wonterghem, B., Schäfer, F. P. & Sauerbrey, R. Angle-dependent X-ray emission and resonance absorption in a laser-produced plasma generated by a high intensity ultrashort pulse. *Physical Review Letters* **70**, 794–797 (1993).

7. Meier, M., Romano, V. & Feurer, T. Material processing with pulsed radially and azimuthally polarized laser radiation. *Applied Physics A* **86**, 329–334 (2006).

8. Lou, K. *et al.* Femtosecond laser processing by using patterned vector optical fields. *Sci. Rep.* **3**, 2281 (2013).

9. Jang, J.-H. *et al.* 3D micro- and nanostructures via interference lithography. *Adv. Funct. Mater.* **17**, 3027–3041 (2007).

10. Skoulas, E., Manousaki, A., Fotakis, C. & Stratakis, E. Biomimetic surface structuring using cylindrical vector femtosecond laser beams. *Sci. Rep.* **7**, 45114 (2017).

11. Nivas, J. J. J. *et al.* Direct femtosecond laser surface structuring with optical vortex beams generated by a q-plate. *Sci. Rep.* **5**, 17929 (2015).

12. Lu, J. *et al.* 3d structured Bessel beam polarization and its application to imprint chiral optical properties in silica. *APL Photonics* **8**, 060801 (2023).

13. Toyoda, K., Miyamoto, K., Aoki, N., Morita, R. & Omatsu, T. Using optical vortex to control the chirality of twisted metal nanostructures. *Nano Lett.* **12**, 3645–3649 (2012).

14. Toyoda, K. *et al.* Transfer of light helicity to nanostructures. *Physical Review Letters* **110**, 143603 (2013).

15. Ablez, A., Toyoda, K., Miyamoto, K. & Omatsu, T. Microneedle structuring of si(111) by irradiation with picosecond optical vortex pulses. *Applied Physics Express* **13**, 062006 (2020).

16. Syubaev, S. *et al.* Chirality of laser-printed plasmonic nanoneedles tunable by tailoring spiral-shape pulses. *Applied Surface Science* **470**, 526–534 (2019).

17. Ablez, A., Toyoda, K., Miyamoto, K. & Omatsu, T. Nanotwist of aluminum with irradiation of a single optical vortex pulse. *OSA Continuum* **4**, 403–408 (2021).

18. Yoo, J.-H. *et al.* Directed dewetting of amorphous silicon film by a donut-shaped laser pulse. *Nanotechnology* **26**, 165303 (2015).

19. Ni, J. *et al.* Three-dimensional chiral microstructures fabricated by structured optical vortices in isotropic material. *Light: Science & Applications* **6**, e17011 (2017).

20. Lee, J. *et al.* Photopolymerization with light fields possessing orbital angular momentum: Generation of helical microfibers. *ACS Photonics* **5**, 4156–4163 (2018).

21. Durnin, J., Miceli, J. J. & Eberly, J. H. Diffraction-free beams. *Physical Review Letters* **58**, 1499–1501 (1987).

22. Duocastella, M. & Arnold, C. Bessel and annular beams for materials processing. *Laser & Photonics Reviews* **6**, 607–621 (2012).

23. Herman, R. M. & Wiggins, T. A. Production and uses of diffractionless beams. *J. Opt. Soc. Am. A* **8**, 932–942 (1991).

24. Froehly, L., Jacquot, M., Lacourt, P. A., Dudley, J. M. & Courvoisier, F. Spatiotemporal structure of femtosecond Bessel beams from spatial light modulators. *J. Opt. Soc. Am. A Opt. Image Sci. Vis.* **31**, 790–793 (2014).

25. Polesana, P., Franco, M., Couairon, A., Faccio, D. & Di Trapani, P. Filamentation in Kerr media from pulsed Bessel beams. *Phys. Rev. A* **77** (2008).

26. Bhuyan, M. K. *et al.* Ultrafast laser nanostructuring in bulk silica, a “slow” microexplosion. *Optica* **4**, 951 (2017).

27. Courvoisier, F. Nonstandard light for ultrafast laser microstructuring and nanostructuring. In *Springer Series in Optical Sciences*, Springer series in optical sciences, 581–621 (Springer International Publishing, Cham, 2023).

28. Bhuyan, M. *et al.* High aspect ratio nanochannel machining using single shot femtosecond Bessel beams. *Applied Physics Letters* **97**, 081102–081102 (2010).

29. Rapp, L. *et al.* High aspect ratio micro-explosions in the bulk of sapphire generated by femtosecond Bessel beams. *Sci. Rep.* **6**, 34286 (2016).

30. Jenne, M. *et al.* High-quality tailored-edge cleaving using aberration-corrected Bessel-like beams. *Optics Letters* **43**, 3164 (2018).

31. Stoian, R. & Colombier, J. P. Advances in ultrafast laser structuring of materials at the nanoscale. *Nanophotonics* **9**, 4665–4688 (2020).

32. Flamm, D. *et al.* Structured light for ultrafast laser micro- and nanoprocessing. *Optical Engineering* **60** (2021).

33. Aghdami, K. M., Rahnama, A., Ertorer, E. & Herman, P. R. Laser nano-filament explosion for enabling open-grating sensing in optical fibre. *Nature Communications* **12** (2021).

34. Jukna, V. *et al.* Filamentation with nonlinear Bessel vortices. *Optics Express* **22**, 25410 (2014).

35. Gamaly, E. G. & Rode, A. V. Physics of ultra-short laser interaction with matter: From phonon excitation to ultimate transformations. *Prog. Quantum Electron.* **37**, 215–323 (2013).

36. Wang, G. *et al.* Cylindrical shockwave-induced compression mechanism in femtosecond laser Bessel pulse micro-drilling of PMMA. *Applied Physics Letters* **110**, 161907 (2017).

37. Xie, C. *et al.* Tubular filamentation for laser material processing. *Scientific Reports* **5**, 8914 (2015).

38. del Hoyo, J., Meyer, R., Furfaro, L. & Courvoisier, F. Nanoscale confinement of energy deposition in glass by double ultrafast Bessel pulses. *Nanophotonics* **10**, 1089–1097 (2021).

39. Ardaneh, K. *et al.* High energy density plasma mediated by collisionless resonance absorption inside dielectrics arXiv.2109.00803 (2022).

40. Rethfeld, B., Ivanov, D. S., Garcia, M. E. & Anisimov, S. I. Modelling ultrafast laser ablation. *Journal of Physics D: Applied Physics* **50**, 193001 (2017).

41. Vailionis, A. *et al.* Evidence of superdense aluminium synthesized by ultrafast microexplosion. *Nature Communications* **2** (2011).

42. Rahimian, M. *et al.* Polarization dependent nanostructuring of silicon with femtosecond vortex pulse. *APL Photonics* **2**, 086104 (2017).

43. Chen, T. *et al.* Nano-spheroid formation on YAG surfaces induced by single ultrafast Bessel laser pulses. *Applied Surface Science* **604**, 154360 (2022).

44. Lu, Y. *et al.* Nanochannels with a 18-nm feature size and ultrahigh aspect ratio on silica through surface assisting material ejection. *Advanced Photonics Nexus* **1**, 026004 (2022).

45. Dobrovinskaya, E. R., Lytvynov, L. A. & Pishchik, V. *Sapphire*. Micro- and Opto-Electronic Materials, Structures, and Systems (MOEM) (Springer, 2009).

46. Lin, S. P. & Reitz, R. D. Drop and spray formation from a liquid jet. *Annual Review of Fluid Mechanics* **30**, 85–105 (1998).

47. Kuznetsov, A., Unger, C., Koch, J. & Chichkov, B. Laser-induced jet formation and droplet ejection from thin metal films. *Applied Physics A* **106** (2012).

48. Li, Q., Alloncle, A., Grojo, D. & Delaporte, P. Laser-induced nano-jetting behaviors of liquid metals. *Applied Physics A* **123**, 718 (2017).

49. Takahashi, F. *et al.* Picosecond optical vortex pulse illumination forms a monocrystalline silicon needle. *Scientific Reports* **6**, 21738 (2016).

50. Eggers, J. Nonlinear dynamics and breakup of free-surface flows. *Reviews of Modern Physics* **69**, 865–929 (1997).

51. Vágó, N., Spiegel, A., Couty, P., Wagner, F. & Richerzhagen, B. New technique for high-speed microjet breakup analysis. *Experiments in Fluids* **35**, 303–309 (2003).

52. Musgraves, J. D., Hu, J. & Calvez, L. (eds.) *Springer Handbook of Glass*. Springer Handbooks (Springer International Publishing, Cham, Switzerland, 2019), 1 edn.

53. Kowalewski, T. On the separation of droplets from a liquid jet. *Fluid Dynamics Research* **17**, 121–145 (1996).

54. Juodkazis, S. *et al.* Laser-induced microexplosion confined in the bulk of a sapphire crystal: Evidence of multimegabar pressures. *Phys. Rev. Lett.* **96**, 166101 (2006).

55. Ghassemieh, E., Versteeg, H. & Acar, M. The effect of nozzle geometry on the flow characteristics of small water jets. *Archive Proceedings of the Institution of Mechanical Engineers Part C Journal of Mechanical Engineering Science 1989-1996 (vols 203-210)* **220** (2006).

56. Reitz, R. Modeling atomization processes in high-pressure vaporizing sprays. *Atomisation Spray Technology* **3**, 309–337 (1987).

57. Eggers, J. & Villermaux, E. Physics of liquid jets. *Rep. Prog. Phys.* **71**, 036601 (2008).

58. Duocastella, M., Fernández-Pradas, J. M., Morenza, J. L. & Serra, P. Time-resolved imaging of the laser forward transfer of liquids. *J. Appl. Phys.* **106**, 084907 (2009).

59. Iwasawa, Y. & Abe, Y. Scaling analysis of melt jets and solidification modes. *Annals of Nuclear Energy* **125**, 231–241 (2019).

60. Nesterov, A. V. & Niziev, V. G. Laser beams with axially symmetric polarization. *Journal of Physics D: Applied Physics* **33**, 1817 (2000).

61. Papadopoulos, A., Skoulas, E., Tsibidis, G. & Stratakis, E. Formation of periodic surface structures on dielectrics after irradiation with laser beams of spatially variant polarisation: a comparative study. *Applied Physics A* **124**, 146 (2018).

62. Elbersen, R., Vijselaar, W., Tiggelaar, R. M., Gardeniers, H. & Huskens, J. Effects of pillar height and junction depth on the performance of radially doped silicon pillar arrays for solar energy applications. *Advanced Energy Materials* **6**, 1501728 (2016).

63. Singh, V., Nagaraju, J. & Avasthi, S. Radial junction silicon solar cells with micro-pillar array and planar electrode interface for improved photon management and carrier extraction. *Current Applied Physics* **19** (2018).

64. Tanaka, Y. *et al.* Demonstration of a PDMS-based bio-microactuator using cultured cardiomyocytes to drive polymer micropillars. *Lab on a chip* **6**, 230—235 (2006).

65. Chiappini, C. *et al.* Tutorial: using nanoneedles for intracellular delivery. *Nature Protocols* **16**, 4539—4563 (2021).

66. Reitzenstein, S. & Forchel, A. Quantum dot micropillars. *Journal of Physics D- Applied Physics* **43** (2010).

67. Doster, J., Hönl, S., Lorenz, H., Paulitschke, P. & Weig, E. Collective dynamics of strain-coupled nanomechanical pillar resonators. *Nature Communications* **10** (2019).

Supplementary Information for

Single shot generation of high-aspect-ratio nano-rods from sapphire by ultrafast first order Bessel beam

Valeria Viviana Belloni [1] (*), Mostafa Hassan [1], Luca Furfaro [1], Remo Giust [1], Anne-Magali Seydoux-Guillaume [2], Sergio Sao-Joao [3], and Francois Courvoisier [1](*)

[1] FEMTO-ST institute, Univ. Franche-Comté and CNRS, 15B avenue des Montboucons, 25030 Besançon, France.
[2] UJM, CNRS, LGL-TPE, F-42023, Saint Etienne, France
[3] Mines Saint-Etienne, Univ. Lyon, CNRS, UMR 5307 LGF, Centre SMS, F-42023 Saint-Etienne, France

* Corresponding authors: valeria.belloni@femto-st.fr; francois.courvoisier@femto-st.fr

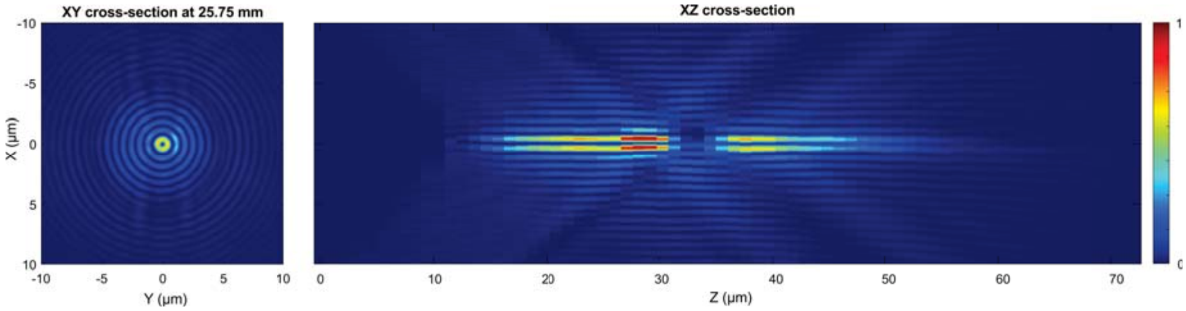

Figure S.1: Fluence distribution of the Bessel beam. (left) Transverse cross-section; (right) longitudinal cross-section. The fluence drop at the propagation distance of 33 μm is due to the singularity at the center of the radial polarization converter.

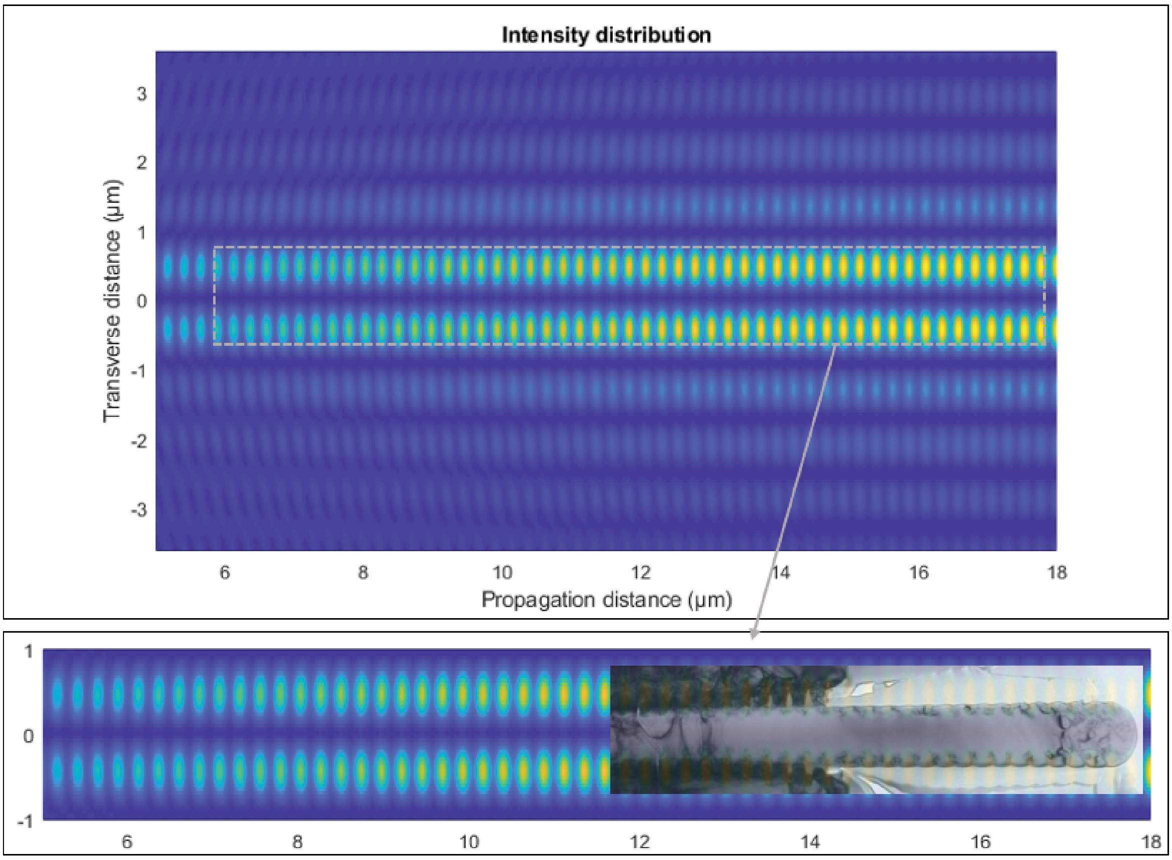

Figure S.2: Simulation of the interference pattern generated by the reflection of the input beam on the exit surface. The simulation is based on plane wave spectrum propagation within the scalar approximation. In the simulation, the exit surface is placed at a propagation distance of $18\,\mu\mathrm{m}$ from the onset of the Bessel beam. Overall, the cylindrical focus (main intensity lobe) of the Bessel beam has been split by the interference into a series of high-intensity torus distributed periodically along the optical axis. The bottom panel shows the same distribution together with the TEM image of the nano-pillar shown in Figure 4 to show the high degree of agreement between the corrugations on the rod and below the surface with the intensity distribution.

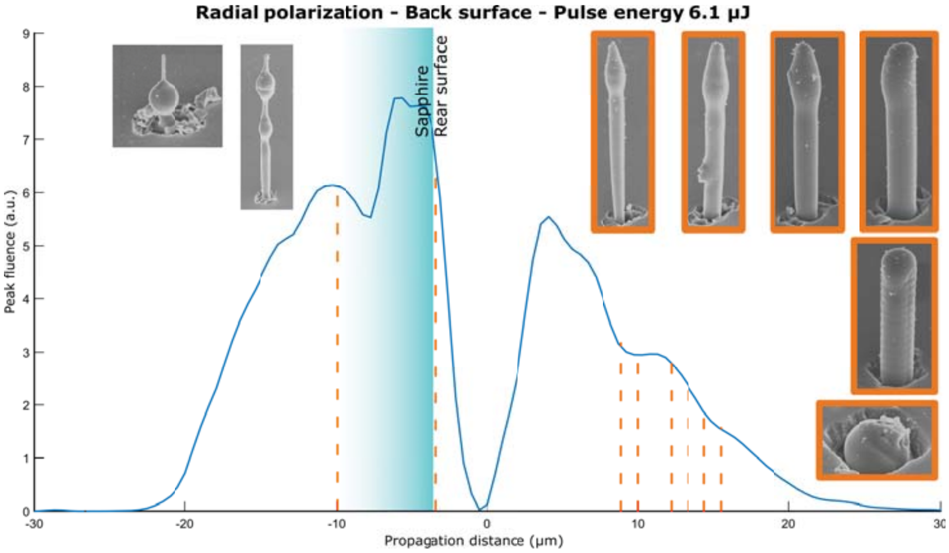

Figure S.3: Different nano-pillar morphologies can be obtained by translating the sample along the beam propagation for the same input pulse energy of 6.1 µJ. The solid blue line shows the profile of the fluence of the main ring of the Bessel beam, for radial polarization, and a pulse duration of 115 fs. Here, the processing is performed on the back surface of the sample. The beam propagation is from left to right. The dashed lines represent at which position of the processed surface a nano-pillar is produced. The SEM images of the nano-pillars at each position are displayed following the sample position. The bottom left image corresponds to the most negative position, while the bottom right image corresponds to the most positive position. The colored frames indicate which conditions lead to a reproducible regime. The SEM images are not in scale.

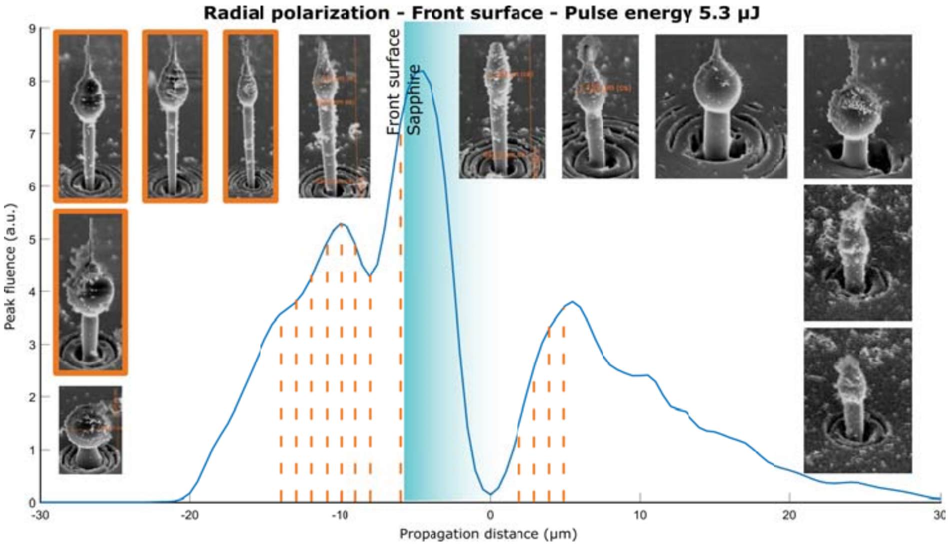

Figure S.4: Different nano-pillar morphologies can be obtained by translating the sample along the beam propagation for the same input pulse energy of 5.3 μJ. The solid blue line shows the profile of the fluence of the main ring of the Bessel beam, for radial polarization, and a pulse duration of 115 fs. Here, the processing is performed on the front surface of the sample. The beam propagation is from left to right. The dashed lines represent at which position of the processed surface a nano-pillar is produced. The SEM images of the nano-pillars at each position are displayed following the sample position. The bottom left image corresponds to the most negative position, while the bottom right image corresponds to the most positive position. The colored frames indicate which conditions lead to a reproducible regime. The SEM images are not in scale.

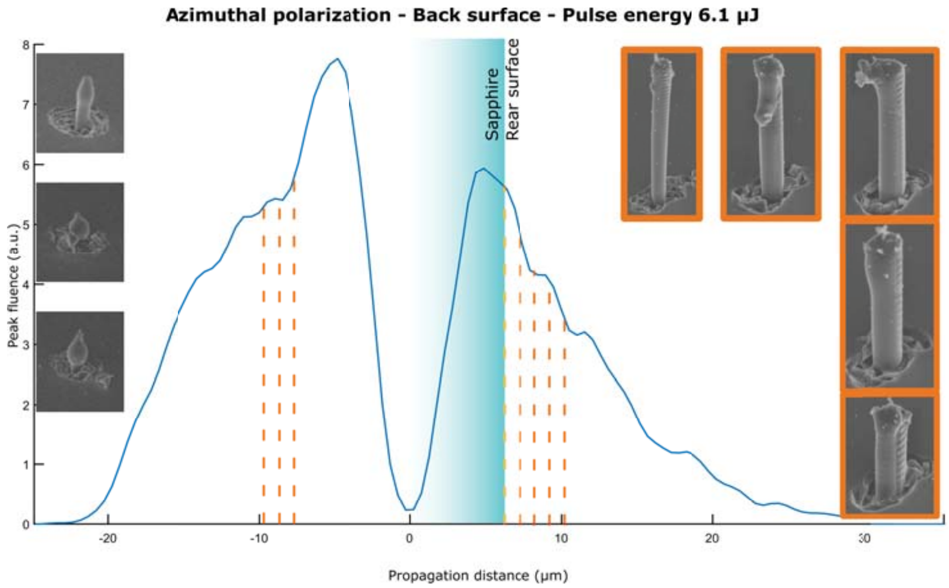

Figure S.5: Different nano-pillar morphologies can be obtained by translating the sample along the beam propagation for the same input pulse energy of 6.1 µJ. The solid blue line shows the profile of the fluence of the main ring of the Bessel beam, for azimuthal polarization, and a pulse duration of 115 fs. Here, the processing is performed on the back surface of the sample. The beam propagation is from left to right. The dashed lines represent at which position of the processed surface a nano-pillar is produced. The SEM images of the nano-pillars at each position are displayed following the sample position. The bottom left image corresponds to the most negative position, while the bottom right image corresponds to the most positive position. The colored frames indicate which conditions lead to a reproducible regime. The SEM images are not in scale.

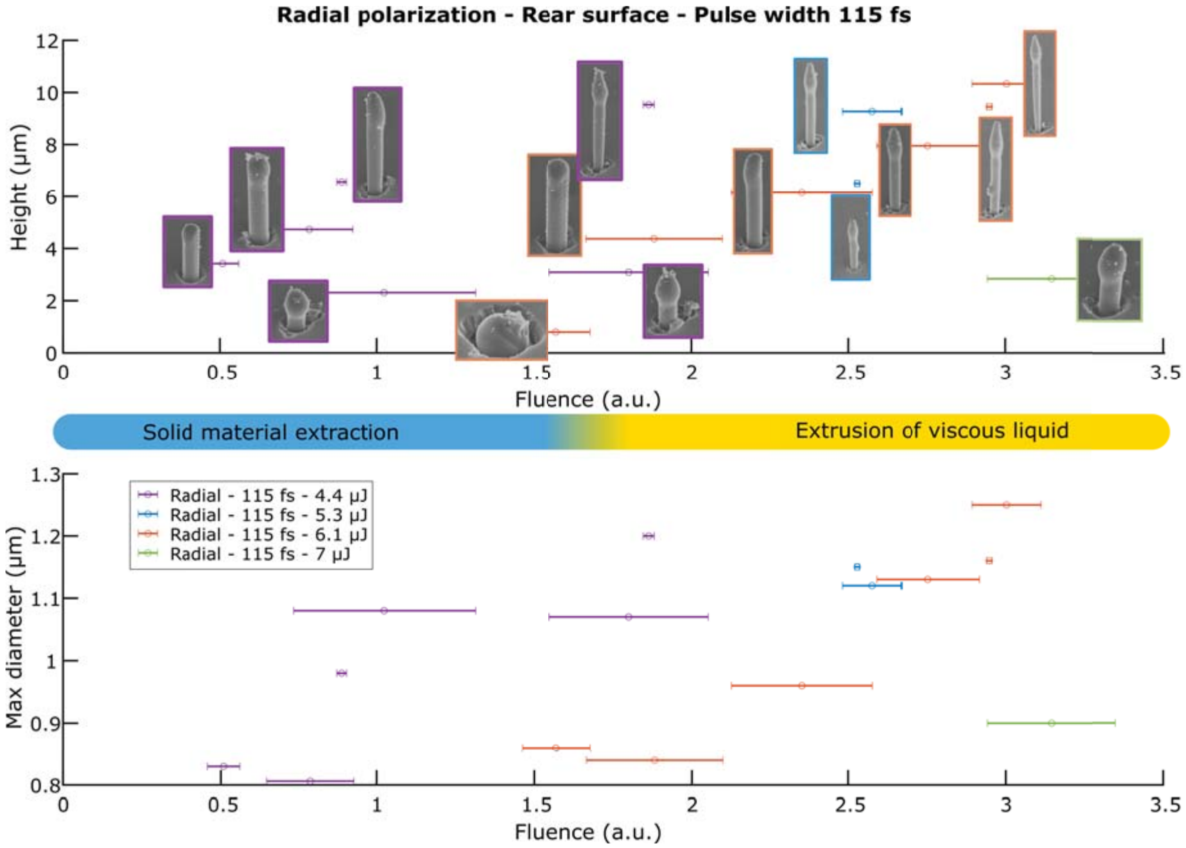

Figure S.6: Height (top panel) and maximum diameter (bottom panel) of the nano-pillars as a function of the fluence of the main Bessel ring on the sample surface. We provide the data only for the reproducible regimes. In this configuration, the beam was radially polarized, with a pulse width of 115 fs and the processing was performed on the rear surface of the sample. Several pulse energies are investigated. In the top panel, SEM images are shown as insets next to their corresponding data point. (Images are not in scale.) We observe the transition from the first regime (solid material extraction) to the second one (extrusion of viscous liquid) for a fluence of ~ 1.7 a.u. (all fluence units across the figures share the same reference).

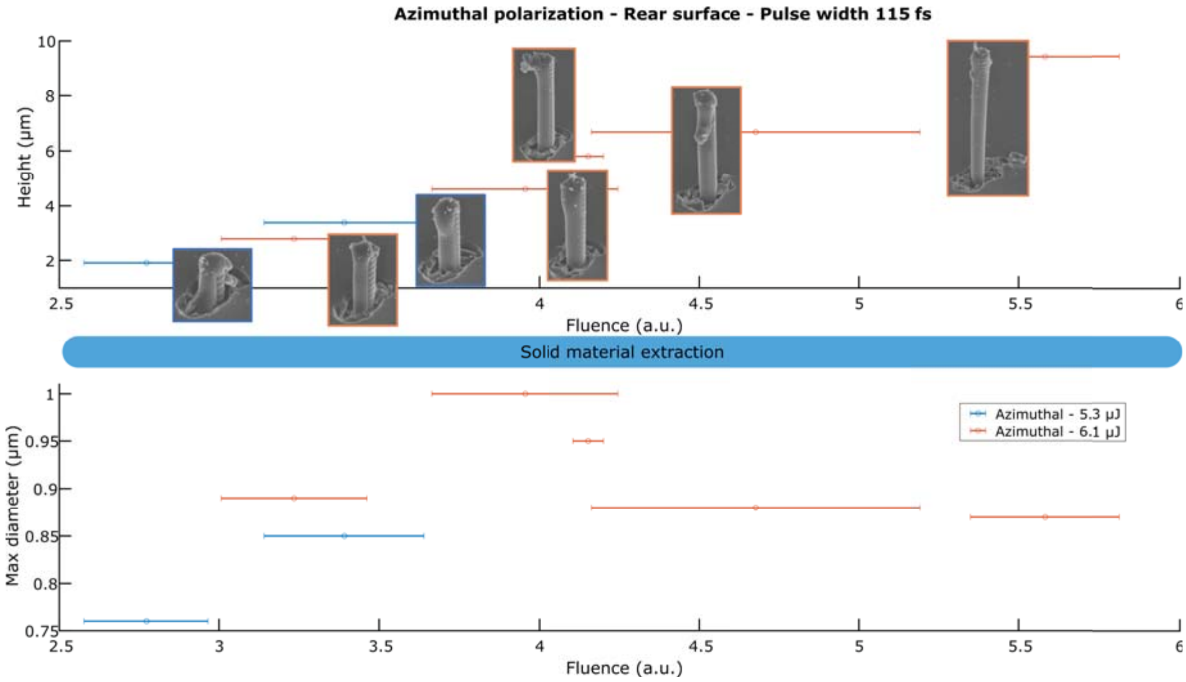

Figure S.7: Height (top panel) and maximum diameter (bottom panel) of the nano-pillars as a function of the fluence of the main Bessel ring on the sample surface (see caption of Figure S.6 for all details). In this configuration, the beam was azimuthally polarized, with a pulse width of 115 fs and the processing was performed on the rear surface of the sample. In this configuration, we observe only the first regime (solid material extraction).

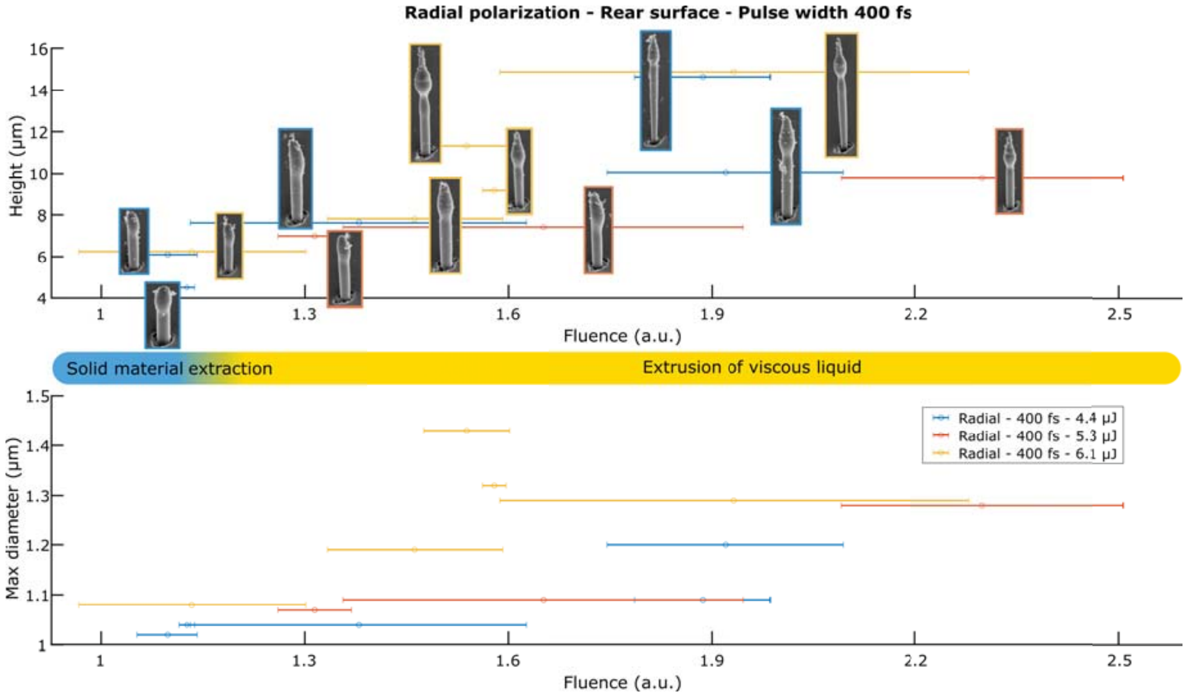

Figure S.8: Height (top panel) and maximum diameter (bottom panel) of the nano-pillars as a function of the fluence of the main Bessel ring on the sample surface (see caption of Figure S.6 for all details). In this configuration, the beam was radially polarized, with a pulse width of 400 fs and the processing was performed on the rear surface of the sample. We observe the transition from the first regime (solid material extraction) to the second one (extrusion of viscous liquid) for a fluence of ~ 1.2 a.u. (all fluence units across the figures share the same reference).

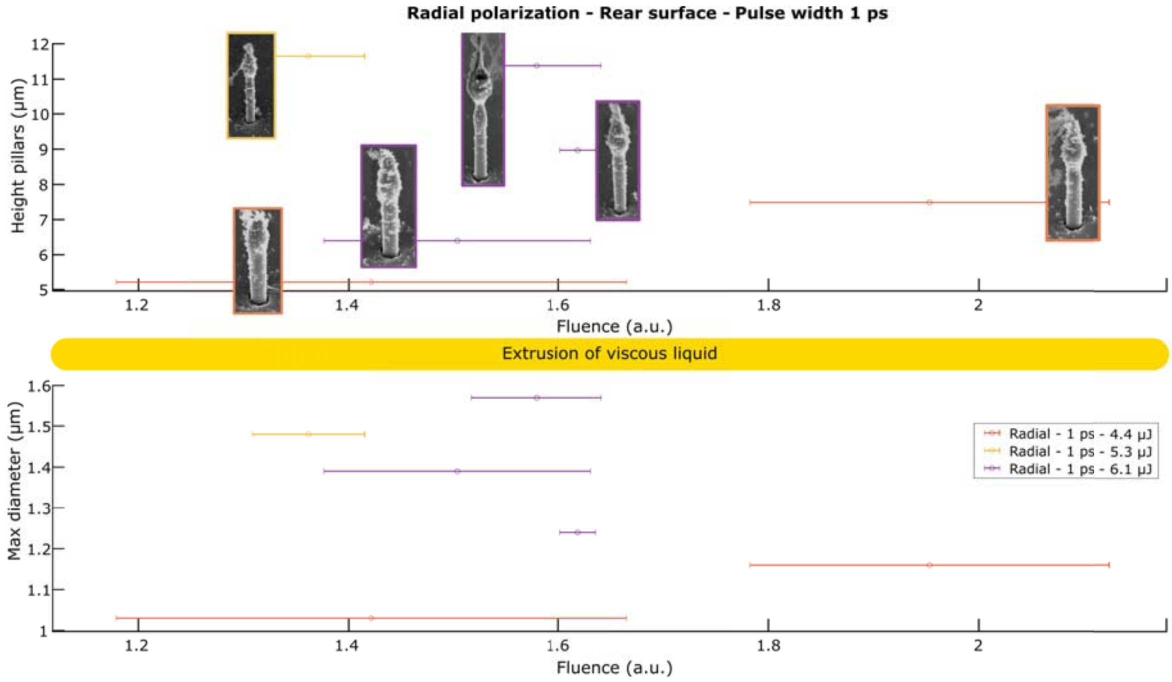

Figure S.9: Height (top panel) and maximum diameter (bottom panel) of the nano-pillars as a function of the fluence of the main Bessel ring on the sample surface (see caption of Figure S.6 for all details). In this configuration, the beam was radially polarized, with a pulse width of 1 ps and the processing was performed on the rear surface of the sample. We observe only the second regime (extrusion of viscous liquid).

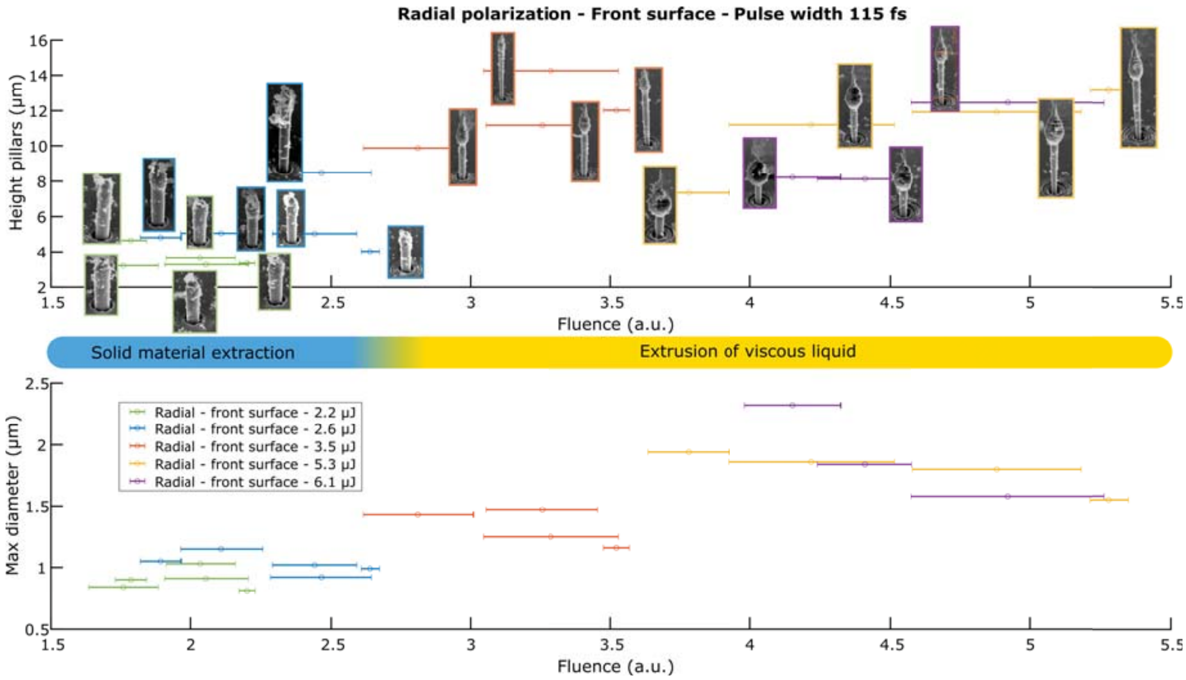

Figure S.10: Height (top panel) and maximum diameter (bottom panel) of the nano-pillars as a function of the fluence of the main Bessel ring on the sample surface (see caption of Figure S.6 for all details). In this configuration, the beam was radially polarized, with a pulse width of 115 fs and the processing was performed on the front surface of the sample. We observe the transition from the first regime (solid material extraction) to the second one (extrusion of viscous liquid) for a fluence of ~ 2.7 a.u.